Published in Journal of Materials Science, Vol. 49, Iss. 8, pp. 3034-3051, April 2014
http://link.springer.com/article/10.1007%2Fs10853-013-8002-5

Relationship between Space and Time Characteristics of Cavitation Impact Pressures and Resulting Pits in Materials

Jin-Keun Choi*, Arvind Jayaprakash, Anil Kapahi, Chao-Tsung Hsiao, Georges L. Chahine

DYNAFLOW, INC.

10621-J Iron Bridge Road, Jessup, Maryland, USA

1. Abstract

Cavitation erosion studies require a well-defined measure of the aggressiveness of the subject cavitation field. One proposed method of cavitation field strength evaluation is to use pitting tests on a selected material sample subjected to the cavitation field. These relatively short duration tests record pits or permanent deformations from individual cavitation events during the cavitation incubation period. The pitting test results are dependent on the load and the material used in the tests and a good understanding of the pit formation mechanism is required to correlate the loads with the deformations. In this study, finite element numerical simulations are conducted to examine the response of several selected materials to imposed loads representing cavitation events. The magnitude, duration, and spatial extent of the loads are varied, and the effects of these on the material deformations are studied. Next, the effects of material properties, such as yield stress, Young's modulus, and plastic modulus on the pitting characteristics are elucidated. Material responses are found to be drastically different between metals and compliant materials and to depend significantly on load duration and spatial extent in addition to the magnitude.

Key words: cavitation, pitting, erosion, impact load, numerical modeling, metal alloys, compliant material

Published in Journal of Materials Science, Vol. 49, Iss. 8, pp. 3034-3051, April 2014
http://link.springer.com/article/10.1007%2Fs10853-013-8002-5

2. Introduction

Cavitation erosion is a mechanical process resulting from local high amplitude short duration loads from the successive collapse of individual and collective cavities [1]. The overall picture is that bubble nuclei in the liquid grow explosively in low pressure regions forming cavitation bubble clouds [1-6]. These subsequently collapse generating very high local pressures and temperatures [7,8]. When the bubbles are very close to or at a material surface, micro reentrant jets are formed during the collapse following large bubble deformations, vector towards the material, and impact its surface [9-11]. When the pressure load exceeds the elastic limit of the material, the material locally undergoes permanent deformation leaving microscopic pits [12]. This initial phase of material response to the cavitation field or incubation period does not involve any mass loss. With repeated impacts, hardening of the material surface layer develops, pits accumulate, and finally micro-failures occur resulting in material removal and weight loss.

Materials resistance to cavitation erosion is often studied using laboratory accelerated erosion tests since real scale erosion on well-designed machinery occurs over a long period of time. In the accelerated erosion tests, material samples are subjected to a cavitation field that produces measurable erosion over a short period of time. This, by definition, involves different characteristics of the cavitation field than what is present in the actual flow field the tested material is destined to survive. A practical approach is to assume the laboratory determined ranking of the materials in the accelerated erosion tests will hold in the real application. However, evidence exists that this may not always be the case, since some materials respond differently to cavitation fields of different strengths [13-16]. In order to characterize cavitation erosion for different cavitation conditions, a well-defined method to evaluate the cavitation field strength is needed.

One proposed method to measure the cavitation field strength is to conduct pitting tests, i.e. short duration cavitation tests during the initial erosion incubation period, where non-overlapping pits are produced, then measured and characterized [13]. In pitting tests, the material is used as a recorder of the *highest pressures* in the cavitating field, since each material acts as a high pass filter and records as pits only the cavitating field pressure peaks that result in stresses exceeding the material yield stress and in material permanent plastic deformation. Observation of pits for the purpose of evaluating the cavitation field intensity dates back to the early 1900's when Parsons and Cook [17] observed the depth and dimensions of the pitted areas, and researchers reported the pitting locations relative to cavitation cloud shapes and statistics such as the number and the depth of pits [18-20]. Knapp [19-21] introduced the idea that the pits could be used to understand the intensity of the cavitation field. Similar ideas of observing pits to represent the cavitation field were used in hydraulic turbine cavitation erosion studies [22], where it was found that cavitation aggressiveness in the full scale is more severe than in the model scale. Recent studies using pitting tests include the use of thin copper foil in order to capture relative small magnitude impacts [23], analysis of pitting to determine the impact loads for a modeling effort for ductile metals [24], evaluation of flow aggressiveness in the study of hydraulic turbine flows [25], and applications to the erosion studies of marine propellers [26,27]. With the advance of modern imaging and micro-measurement technologies, recent studies reveal more details of the pit shapes and statistics [28,29]. However, these studies do not provide a detailed description of the pitting mechanism.

Published in Journal of Materials Science, Vol. 49, Iss. 8, pp. 3034-3051, April 2014
http://link.springer.com/article/10.1007%2Fs10853-013-8002-5

In this paper, a numerical approach is taken to investigate pitting dynamics of several materials from the material mechanics viewpoint. A well-established finite element method code DYNA3D [30,31] is used to model the behavior of various materials including metallic alloys and compliant materials. Idealized cavitation loads corresponding to the collapse of cavitation bubbles and the impact of the resulting microjets on the material for various impulsive pressure amplitudes (peak heights), durations, and spatial extents are used to study the response of materials.

3. Approach

The materials' dynamics in response to loadings which are characteristic of cavitation is studied using the finite element model, DYNA3D, initially developed by the Lawrence Livermore National Laboratory [30,31]. DYNA3D is a non-linear explicit solid and structural dynamics solver. Based on a lumped mass formulation it solves the structure momentum equation:

$$\mathbf{M\ddot{U} + C\dot{U} + KU = F}, \tag{1}$$

where $\mathbf{U}$ is the displacement vector, $\mathbf{C}$ is the damping matrix, $\mathbf{K}$ is the stiffness matrix, and $\mathbf{F}$ is the matrix of the applied loads on the structure. DYNA3D is appropriate for problems where high strain rate dynamics or stress wave propagation effects are important. Many material models are available to represent a wide range of material behavior, including elasticity, plasticity, thermal effects, rate dependence, damage, and failure of elements.

3.1. Material Models Used

In this study, two metal alloys (Aluminum 7075 and Stainless Steel A2205), two rubbers, and a polyurea based coating were examined. The alloys were modeled as elastic-plastic with two linear slopes (moduli), one for the initial elastic regime (Young's modulus) and the other for the plastic regime (tangent modulus). The parameters of the model used in this study are shown in Table 1.

We used Blatz-Ko's hyper-elastic model for the two rubbers of different strength with parameters shown in Table 2 [31]. The properties of the rubber #1 are those of typical Neoprene synthetic rubber, and the rubber # 2 is typical Polyurethane. The rubber #1 is about three times stiffer than the rubber #2. The Polyurea material (made from Versalink P-1000 and Isonate 2143L, [32]) was modeled using a viscoelastic model with the following equation for the time dependent shear modulus, G:

$$G(t) = G_\infty + (G_0 - G_\infty)e^{-\beta t}, \tag{2}$$

with

$$G_\infty = 41.3\,MPa, \quad G_0 = 79.1\,MPa, \quad \beta = 15{,}600\,s^{-1}, \quad K = 4.948\,GPa. \tag{3}$$

Here, the time dependence of G is considered, while the bulk modulus, K, is assumed to be constant. The material parameters in (3) are derived from simplification of the 4th order Prony series given in [32], taking the second term as being the major contributor.

Published in Journal of Materials Science, Vol. 49, Iss. 8, pp. 3034-3051, April 2014
http://link.springer.com/article/10.1007%2Fs10853-013-8002-5

Metallic Alloys	Yield Stress (MPa)	Young's Modulus (GPa)	Tangent Modulus (MPa)	Elongation at Break	Density (g/cm^3)
Al 7075	503	71.7	670	0.11	2.81
A2205	515	190	705	0.35	7.88

Table 1. Material properties of the metal alloys simulated in this study.

Compliant Material	Shear Modulus (MPa)	Young's Modulus (MPa)	Density (g/cm^3)
Rubber # 1 (Neoprene)	99.7	292	1.18
Rubber # 2 Polyurethane	34.17	100	1.20

Table 2. Material properties of the rubbers simulated in this study [33,34].

3.2. Cavitation Loads

Two types of loading on the material in a cavitation environment have been identified by researchers. The first type corresponds to shock waves emitted from the collapsing cavities or bubble clouds. The pressure field of this shock wave can be considered as a spherical shock emanating from the bubbles location. The second results from high speed reentrant jets that penetrate microbubbles collapsing very close to the material boundary and hit the material surface. Our previous numerical and experimental studies [35,36] indicate that these pressures can be represented well with a Gaussian distribution in space and time. Figure 1 shows that an experimentally recorded pressure pulse under a cavitating jet can be fitted well using a Gaussian pressure pulse. The same can be also observed under ultrasonic and hydrodynamic cavitation conditions. Thus, in this paper, we idealize the time and space varying impact pressure loading, $P(r,t)$, as follows:

$$P(r,t) = P_0 e^{-\left(\frac{t}{\Delta t}\right)^2} e^{-\left(\frac{r}{\Delta r}\right)^2}, \tag{4}$$

where P_0 is the amplitude of the pressure pulse, Δt is the characteristic loading duration, and Δr is the characteristic radius of the loading footprint. Figure 2 shows a 3D plot representation of the loading prescribed by (4).

Published in Journal of Materials Science, Vol. 49, Iss. 8, pp. 3034-3051, April 2014
http://link.springer.com/article/10.1007%2Fs10853-013-8002-5

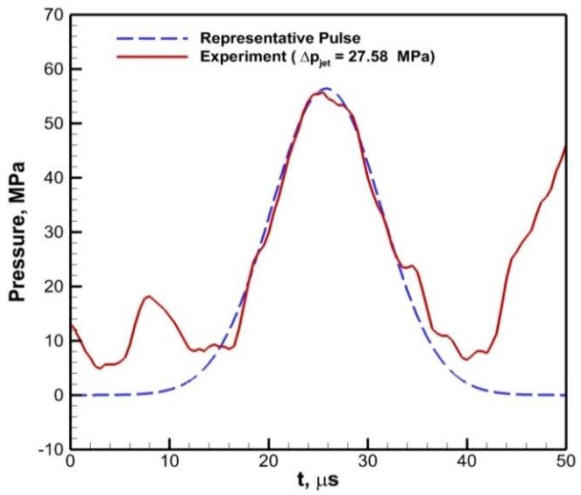

Figure 1. Zoom on a peak of the pressure signal measured in the intense cavitation field due to a cavitating jet (red curve), and representation of a single event cavitation loading using a Gaussian function (blue curve). Reproduced from [36] with permission of ASME.

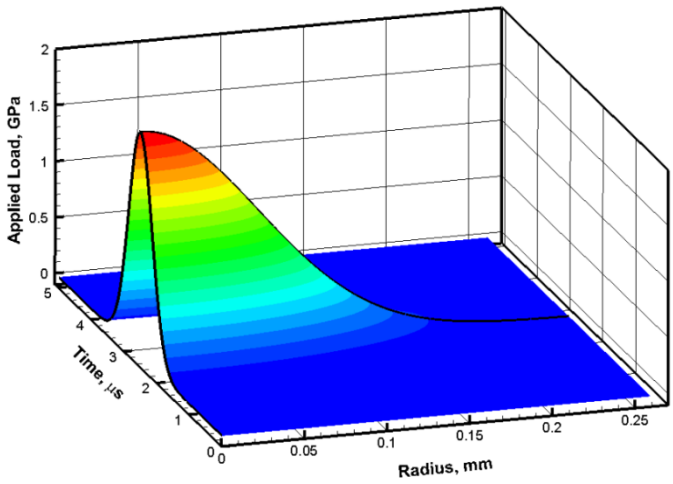

Figure 2. Representation as a double Gaussian (4) of the time and space variation of an impulsive pressure due to a simple bubble collapse. Only half the space domain is shown to visualize the time evolution of the load. P_0 = 2 GPa, Δt = 0.5 μs, Δr = 100 μm.

The various materials presented above were modeled in DYNA3D using rectangular brick elements as shown in Figure 3. A stretched grid mesh of the one quarter of the computational domain of size 1 cm x 1 cm x 0.5 cm was used to represent the material. Two planes of symmetry were used, and the mesh was concentrated near the symmetry planes and near the top surface where the pressure loading was applied. The finest mesh size was a 5 μm x 5 μm x 5 μm cube. The bottom boundary of the domain was rigidly supported, and symmetry conditions were applied to the two symmetry planes. At the far side boundaries, a free (or zero loading) condition was applied.

Published in Journal of Materials Science, Vol. 49, Iss. 8, pp. 3034-3051, April 2014
http://link.springer.com/article/10.1007%2Fs10853-013-8002-5

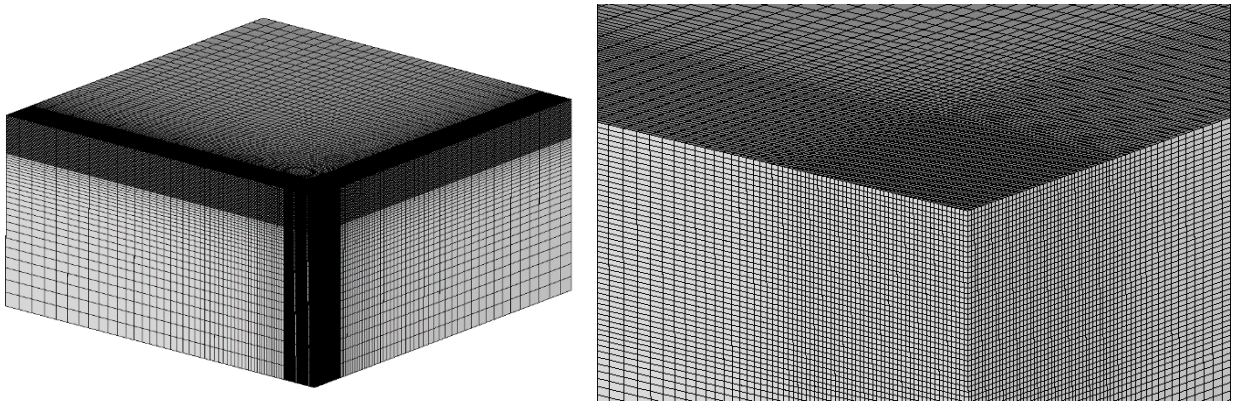

Figure 3. Mesh used in the modeling of various materials response to the loading from a single cavitation event. Full view (left) and zoomed view (right). The dimensions of the modeled quarter domain were 1 cm x 1 cm x 0.5 cm. Two symmetry planes were used (i.e. the full simulation was for a 2 cm x 2cm x 0.5 cm volume). The finest mesh size was 5 μm.

4. Materials Response to the Loads

In order to study the influence of the various load parameters (defined in the preceding section), which affect the material response and subsequently the pit depth, a set of parametric simulations were conducted. Typical load ranges based on our numerical and experimental studies of cavitation erosion [36,37], were used. These were as follows: pressure load amplitudes between 1 MPa and 2 GPa, load durations between 0.1 μs and 2 μs, and load spatial footprints of radii between 10 μm and 100 μm.

4.1. Effect of Collapse Pressure Amplitude

The effect of the amplitude of the pressure due to bubble collapse on the pit formation is investigated first. Two different ranges of collapse pressure amplitudes (one for alloys and one for compliant materials) were selected to capture the dynamics of each class of material properly as the metals are much stiffer than the compliant materials. The compliant materials were subjected to loads between 1 MPa and 10 MPa, i.e. two orders of magnitude lower than the loads applied to the metallic materials (0.1 GPa to 2.0 GPa). Figure 4 illustrates the Gaussian loads applied on the metallic alloys, where collapse pressure amplitudes were varied from 0.1 GPa to 2.0 GPa. Note that the beginning of load is shifted such that the maximum loading occurs at time, t = 2.5 μs regardless of the loading duration, which will be varied later. The other two parameters were kept fixed and at the selected values: Δt = 0.1 μs and Δr = 100 μm.

To understand the material response to these Gaussian loads, stress and stain distributions inside the material were computed. Figure 5 (left) shows contours of the effective stress[1] distribution under the impacted surface when the maximum deformation of the material surface

[1] The effective stress, also known as von Mises stress, is $\sigma_v = \sqrt{(3/2)\, s_{ij} s_{ij}}$ where S_{ij} is the deviatoric stress tensor.

center is reached. The highest stresses are observed below the material surface at a depth of the same order as the load radial extent, Δr. Figure 5 (right) shows the equivalent plastic strain[2] distribution at the same time instant. The equivalent strain also achieves a maximum at the same location below the surface.

Figure 6 shows the effective stress (left) and equivalent strain (right) at t = 10 μs, i.e. the end of the computation after the permanent deformation has been reached. The stress contours show the complex distribution of the residual stress permanently left after this pressure load. The strains remaining in the permanently deformed material have a maximum located near the maximum residual stress location. By the time the permanent deformation was reached, the location of the maximum residual stress and strain has moved a little deeper into the material compared to the location at maximum load (t = 2.5 μs).

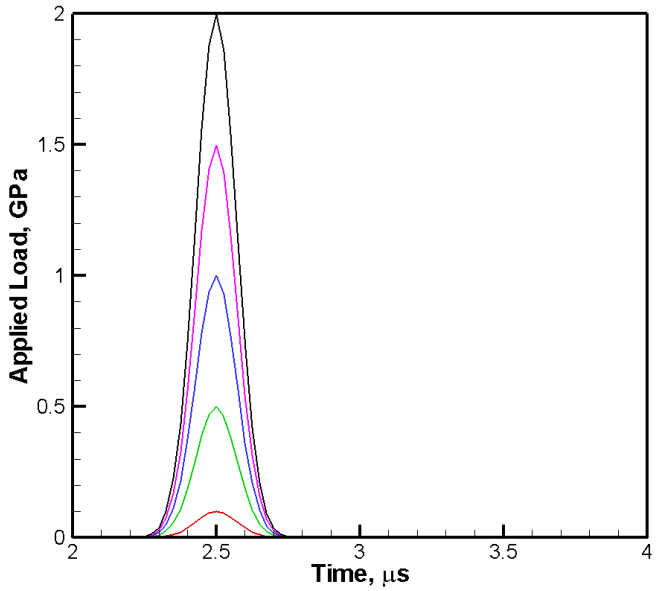

Figure 4. Illustration of the applied Gaussian loading to study the effect of varying the load amplitude. The other two parameters, load duration, Δt and load foot print radios Δt were maintained the same: Δt = 0.1 μs, Δr = 100 μm.

[2] The equivalent plastic strain is defined as $\varepsilon_v = \int_0^t d\varepsilon_v$, $d\varepsilon_v = \sqrt{(2/3)d\varepsilon_{ij}d\varepsilon_{ij}}$, where $d\varepsilon_{ij}$ is the incremental plastic strain tensor.

Published in Journal of Materials Science, Vol. 49, Iss. 8, pp. 3034-3051, April 2014
http://link.springer.com/article/10.1007%2Fs10853-013-8002-5

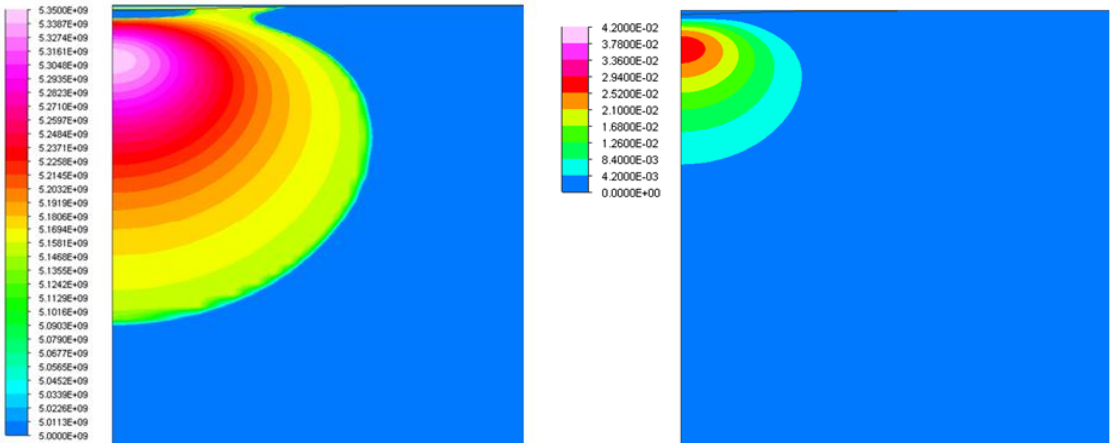

Figure 5. Effective stress (left) and equivalent plastic strain (right) at t=2.5 μs for the loading function of Δt = 0.25 μs and spatial radial extent of Δr = 200 μm, and amplitude P_0 = 2 GPa on Stainless Steel A2205.

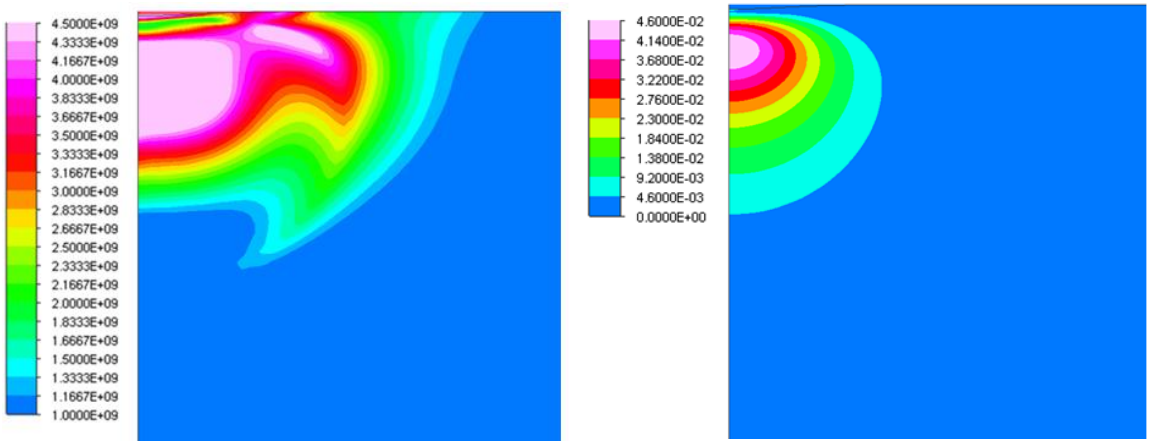

Figure 6. Effective stress (left) and equivalent plastic strain (right) at the end of 10 μs for the loading function of Δt = 0.25 μs and spatial radial extent of Δr = 200 μm, and amplitude P_0 = 2 GPa on Stainless Steel A2205.

The vertical displacement versus time of the center point of the material surface (where the imposed loading was centered) is shown in Figure 7. The motion of this point with time is shown in Figure 7 (a) and (b) for Aluminum A7075 and Stainless Steel A2205 respectively. In both materials, the vertical displacement followed the time variations of the loading curve. The material responded initially in an elastic fashion with the strains being proportional to the imparted stresses. As the load increased toward its maximum, the compressive stress below the surface reached the yield point first (Figure 5). From there on, plastic deformations continued to increase until the maximum load was reached. When the load continued to rise beyond that point, a larger volume of the material proceeded into plastic deformation. Later, when the loading decreases from the maximum value, the material surface either recovered to the original surface (when the loading was small, and plastic deformation did not occur) or retained a

Published in Journal of Materials Science, Vol. 49, Iss. 8, pp. 3034-3051, April 2014
http://link.springer.com/article/10.1007%2Fs10853-013-8002-5

permanent deformation (when the loading was high) leaving a complex distribution of residual stress in the material due to successive reflections of the stress waves at the material surface and bottom (Figure 6).

The time history plots (Figure 7) show that a maximum instantaneous displacement of the center point happens at or slightly after the load maximum. This would be a result of time delay due to stress wave propagation from the top surface down into the material. After the plastic deformation, the unloading occurs over a stress-strain line different than the initial elastic line and a permanent indentation or "pit" remains once the stress is fully relieved. The depth of the final pit depends on both the considered material and on the cavitation load. Also, as described above, permanent pits are only produced when the local effective stresses generated by the load are larger than the yield stress, σ_Y, of the materials.

Figure 8 shows the variations with the applied load magnitude of the plate center point maximum and permanent displacement. For a relatively small load, such as 0.5 GPa and below, the maximum displacement was of the order of 1 to 2 μm, but the surface finally returned to its original location leaving no permanent deformation. For larger loads (1 GPa and above), the maximum displacements increased with the load increases and permanent deformation occurred as the yield stresses of the two materials (503 MPa and 515 MPa) are exceeded. The difference between the maximum and the permanent displacements is observed to be nearly constant for a given material and for high loading. Aluminum 7075 shows a larger difference between the two displacements compared to the Stainless Steel A2205. This is due to the difference in the Young's modulus of the two materials (Table 1). When the material recovers from the plastic deformation, it follows the slope of the Young's modulus. The Young's modulus of Aluminum 7075 (71.7 GPa) is smaller than that of the Stainless Steel A2205 (190 GPa), and thus Aluminum exhibits larger displacement recovery from the maximum deformation for the same load.

Figure 9 (a) compares the pit diameters from the same set of applied load conditions. The pit diameter is defined as the diameter of the material region which is displaced vertically into the material more than 1 μm. The diameters shown in the figure correspond to the two depths shown in Figure 8 and were taken for each condition at two time instances: one at the maximum deformation and the other at the final permanent deformation. The maximum diameters observed on Aluminum 7075 were consistently larger than those of the Stainless Steel A2205 for all loading magnitudes that resulted in deformation (i.e. for load magnitude larger than 0.5 GPa), which is explained by the fact that the Aluminum is softer than the Stainless Steel. However, the resulting permanent pit diameters became much smaller. Only the largest two loading conditions (1.5 and 2.0 GPa) resulted in permanent deformations. Interestingly, these permanent pit diameters are about the same for the two materials and about the diameter of the applied load, i.e. 200 μm (Δr = 100 μm). The pit depth to diameter ratios are compared in Figure 9 (b). As the loading magnitude increased, this ratio increased as well. This means that the pit depth increases faster than the pit diameter as the loading magnitude increases.

Published in Journal of Materials Science, Vol. 49, Iss. 8, pp. 3034-3051, April 2014
http://link.springer.com/article/10.1007%2Fs10853-013-8002-5

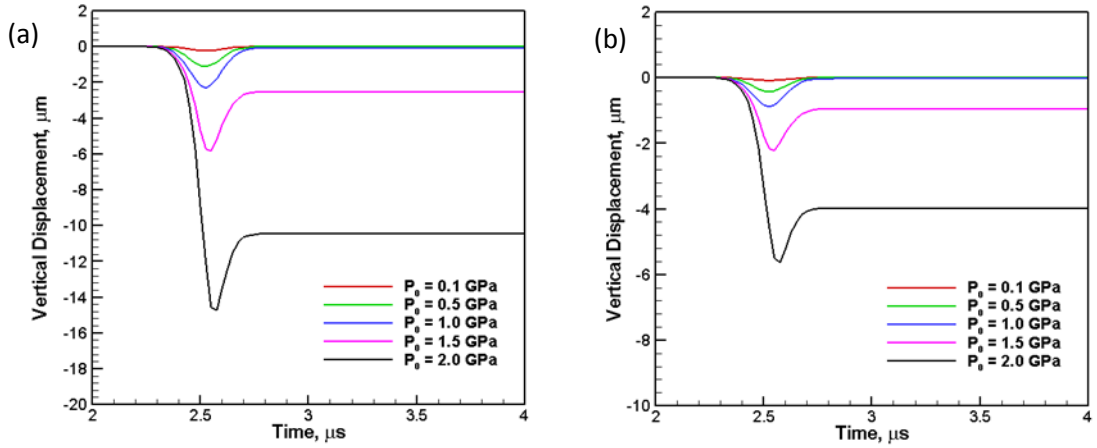

Figure 7. Vertical displacement of the point on the material surface where the center of the loading is located: a) Aluminum Al 7075, b) Stainless Steel A2205. The loading function had the same duration, Δt = 0.1 μs, and spatial radial extent, Δr = 100 μm.

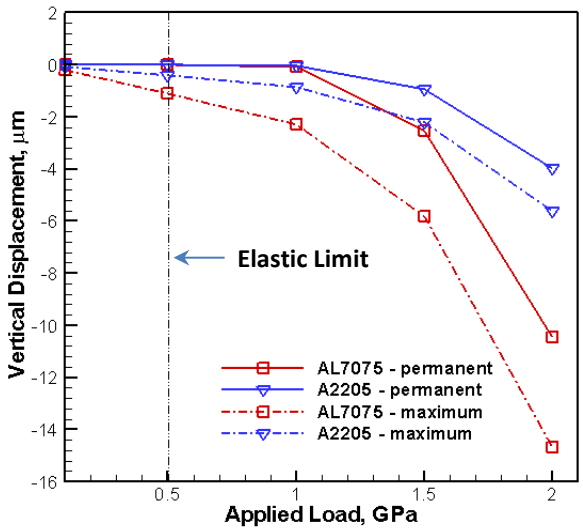

Figure 8. Effect of the magnitude of the cavitation loading on the maximum displacement and permanent deformation for two metallic alloys: Aluminum Al 7075 and Stainless Steel A2205. The loading function had the same duration, Δt = 0.1 μs, and radial extent, Δr = 100 μm.

Published in Journal of Materials Science, Vol. 49, Iss. 8, pp. 3034-3051, April 2014
http://link.springer.com/article/10.1007%2Fs10853-013-8002-5

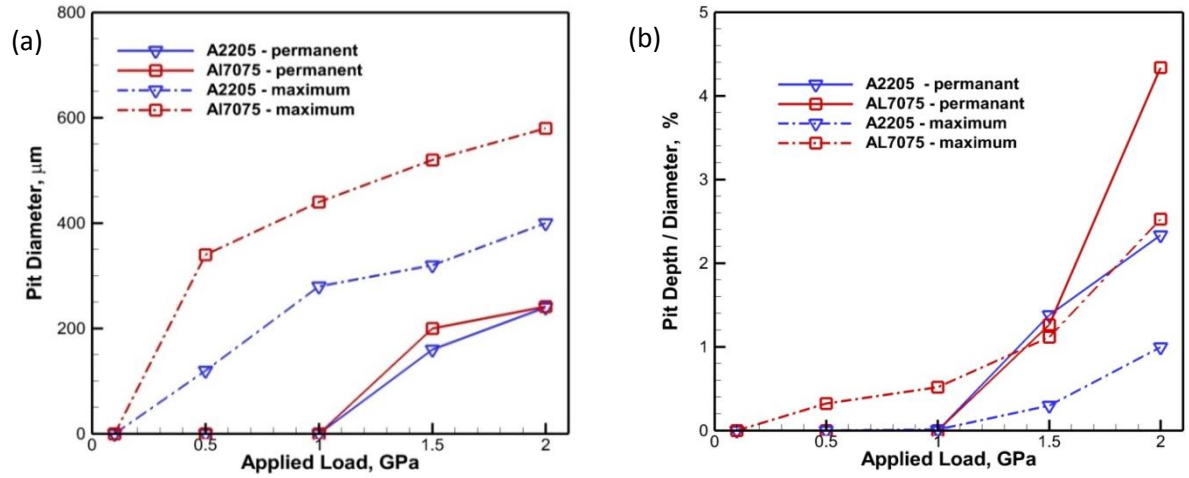

Figure 9. (a) Effect of the magnitude of the cavitation loading on the maximum and permanent diameter of the pit for two metallic alloys: Aluminum Al 7075 and Stainless Steel A2205. (b) Pit depth to diameter ratio. The loading function had the same duration, Δt = 0.1 μs, and spatial radial extent, Δr = 100 μm.

The compliant materials, rubber # 1, rubber # 2, and Polyurea (made from Versalink P-1000 and Isonate 2143L, [32]), were subjected to pressure loadings between 1 MPa and 10 MPa. Figure 10 shows the time history of the plate center vertical displacement for the three compliant materials. Here, we observe no permanent deformation since both hyper-elastic and viscoelastic models do not incorporate any inelastic characteristics of the material behavior. The response of these three compliant materials can be characterized by the maximum elastic dynamic displacement shown in Figure 11. The maximum displacement is roughly proportional to the magnitude of the loads for all three materials. As the rubber #2 is softer than the rubber #1 (Table 2), it shows the largest displacement. Since the time dependent shear modulus of the Polyurea lies in between those of Rubbers #1 and #2, it is reasonable that the Polyurea deforms more than Rubber #1 but less than Rubber #2.

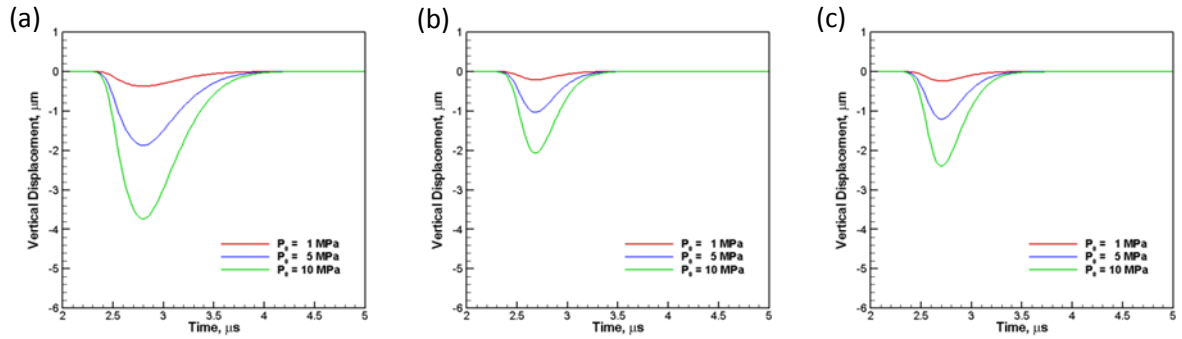

Figure 10. Vertical displacement of the node on the material surface where the center of the loading is located: a) Rubber #1, b) Rubber #2, and c) Polyurea (Versalink P-1000 and Isonate 4143L).. The loading function had the same duration, Δt =0.1 μs, and spatial radial extent, Δr=100 μm.

Published in Journal of Materials Science, Vol. 49, Iss. 8, pp. 3034-3051, April 2014
http://link.springer.com/article/10.1007%2Fs10853-013-8002-5

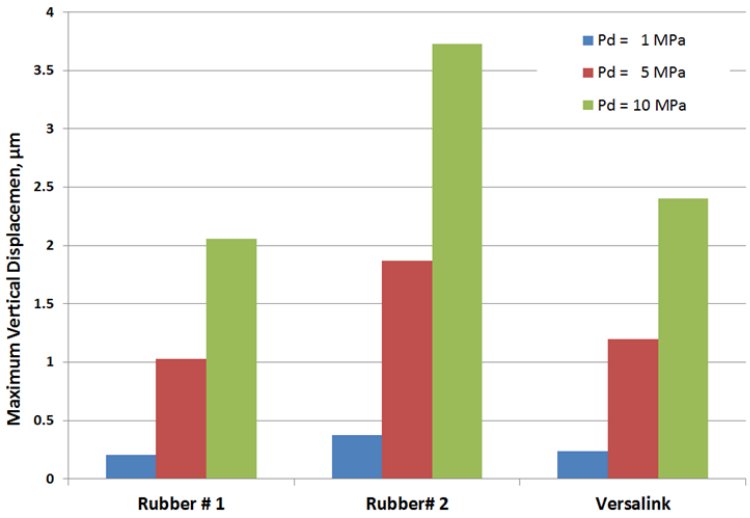

Figure 11. Effect of the magnitude of the cavitation loading on the maximum deformation for the three compliant materials studied: Rubber #1, Rubber #2, and Polyurea (Versalink P-1000 and Isonate 4143L). The loading function had the same duration, Δt = 0.1 µs, and spatial radial extent, Δr = 100 µm.

4.2. Effect of Loading Duration

In order to observe the effects of loading duration, five different loading durations (Δt = 0.1, 0.25, 0.5, 1 and 2 µs) are presented here. All five loadings followed the Gaussian described earlier in (4) and peak to 2 GPa at t = 6 µs. However, the time rates of the loads were different between cases.

The simulated responses of Aluminum 7075 under these loadings are shown in Figure 12 (a). The deformation of the material center point consistently follows the variations of the loading curves during the loading phase. The maximum deformation becomes larger as the duration of the loading is reduced. This would be a result of the inertia of the material, which does not have time to accelerate due to the short duration of the load; the material right under the load is compressed more relative to a slower loading. The recovery of the material also shows significant differences for different loading durations. For long duration loads, $\Delta t \geq 1$ µs, the final displacement (permanent deformation) was about 8 µm and became insensitive to the duration for larger Δt's. However, the short duration cases with $\Delta t < 1$ µs showed larger permanent deformation.

Figure 12 (b) shows the deformation of the center point for Stainless Steel A2205. We observed trends similar to Aluminum 7075 and the deformation followed the timing of the loading curves especially during the loading phase of the material response. Again, the permanent deformations were not sensitive to the duration of the loading for $\Delta t \geq 1$ µs. As the Stainless Steel is stiffer than the Aluminum, the displacements are consistently lower than those of Aluminum.

Published in Journal of Materials Science, Vol. 49, Iss. 8, pp. 3034-3051, April 2014
http://link.springer.com/article/10.1007%2Fs10853-013-8002-5

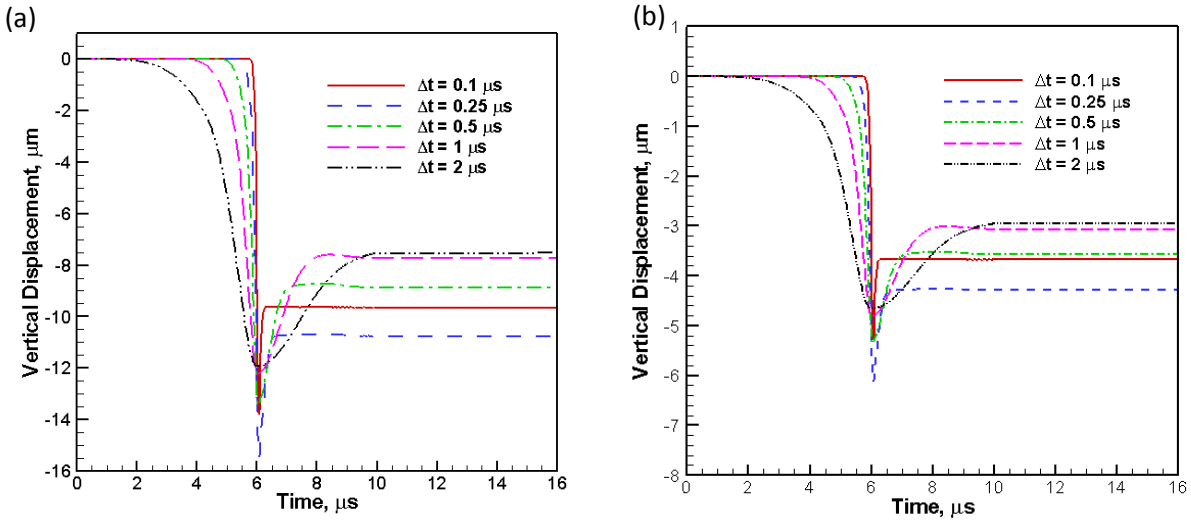

Figure 12. Deformation history of the center point of the metallic alloy materials subjected to the cavitation impulsive loading: a) Aluminum AL7075, and b) Stainless Steel A2205. P_o = 2 GPa, Δr = 100 μm.

Figure 13 shows the trends of the vertical displacement relative to the duration of the load. For both metallic alloys, the vertical displacement approaches an asymptotic value as the duration becomes long. For both Aluminum and Stainless Steel, the largest maximum displacement and the permanent deformation occurred near Δt = 0.25 μs. Since these loads have the same amplitude, short duration loads have less energy than the long duration loads. This explains why the deformation reduces as the load duration becomes shorter than 0.25 μs.

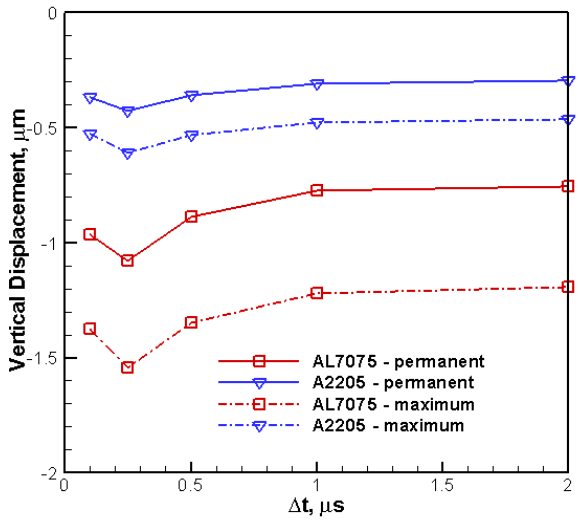

Figure 13. Variation of the maximum and the permanent deformation (pit depth) with the duration of the load for both Aluminum 7075 and Stainless Steel A2205.

Published in Journal of Materials Science, Vol. 49, Iss. 8, pp. 3034-3051, April 2014
http://link.springer.com/article/10.1007%2Fs10853-013-8002-5

Figure 14 shows the displacement curves for the two rubbers and Polyurea. For both rubbers, the maximum displacement depended on the loading duration, and the maximum displacement increases with the duration. However, the rate of the increase diminished with increasing Δt and the amplitude saturated above a Δt of 2 μs. There was no permanent deformation as the rubbers were modeled as hyper-elastic materials which did not have any plastic deformation.

The displacement curves for Polyurea showed a similar trend. The deformation largely followed the loading curves, showing larger maximum displacement with longer durations. There are some final deformation observed at the end of the finite time simulations, but this will eventually goes to zero as the viscoelastic material model does not account for plastic deformation. The time scale of this recovery of the viscoelastic material is much longer than the duration of the presented simulations.

Figure 15 shows how the maximum displacement varies with the duration of the loads. For all three compliant materials, the maximum displacement increased as the duration of the load increased within the range we studied. The increasing trend saturated as the duration becomes long. This trend is very different from what we saw in Figure 13 for the metallic alloys. The trend of the compliant materials looks like the portion of the trends of metals at very small time durations. This may be related to the selected magnitude of the loads relative to the material strength, and further study with larger range of load magnitudes is needed.

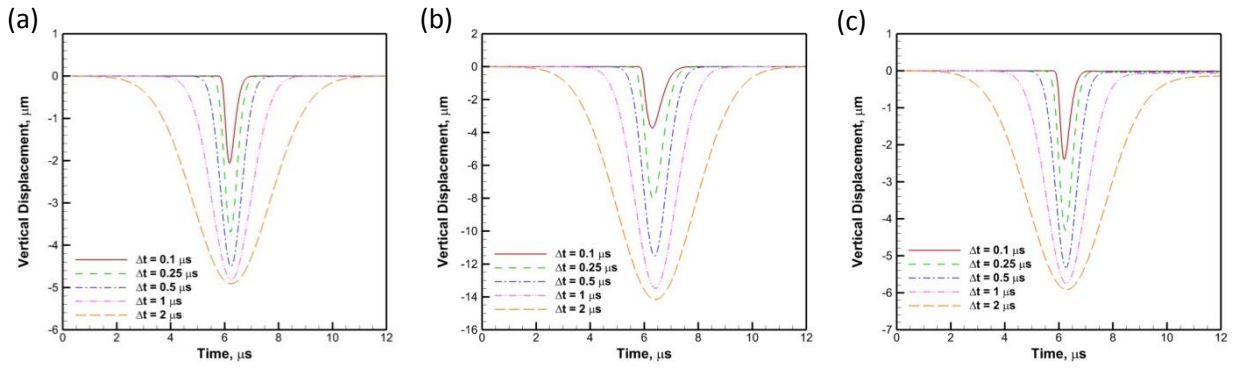

Figure 14. Deformation history of the center point of the soft materials subjected to the cavitation impulsive loading: a) Rubber #1, b) Rubber #2, and c) Polyurea. P_o = 10 MPa, Δr = 100 μm.

Published in Journal of Materials Science, Vol. 49, Iss. 8, pp. 3034-3051, April 2014
http://link.springer.com/article/10.1007%2Fs10853-013-8002-5

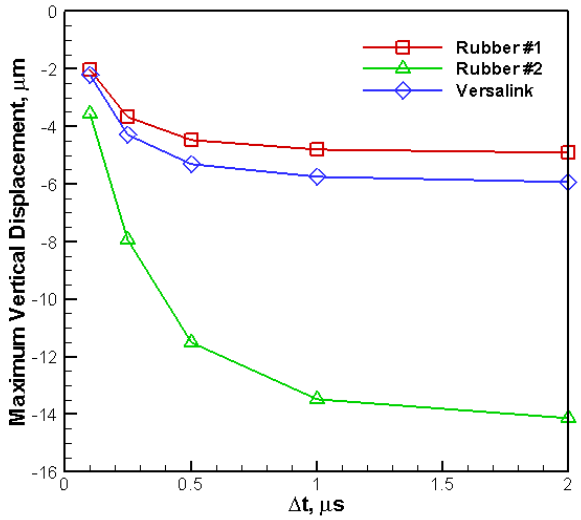

Figure 15. Variation of the maximum deformation with the duration of the load for compliant materials: Rubbers #1 and #2, and Polyurea.

4.3. Effect of Spatial Extent of the Load

In this section, we examine the effect of the loading radial extent, Δr, on the material deformation. The following characteristic radii of the loading, Δr, are presented: 50, 100, 150, 200, and 250 μm. The characteristic loading duration for all the cases was set at 0.1 μs. A peak pressure of 2 GPa was used for the metallic alloy materials, while the compliant materials were subjected to 10 MPa.

The displacement of the center point with time for Aluminum 7075 and Stainless Steel A2205 is shown in Figure 16 for different loading spatial extents. It can be observed that the maximum deformation increases as the radial extent of the loading becomes larger. The final value of the displacement (permanent deformation) also increases with increasing load spatial size and is smaller in the case of Stainless Steel relative to Al 7075. Figure 17 shows the depth of the permanent deformation as a function of the radial extent of the load. For both Aluminum and Stainless Steel, the increase of the pit depth saturates as the radial extent of the load increases.

The loading-unloading cycle of the material as stress-strain curves is shown in Figure 18. The stress-strain curves for Aluminum show that, for larger spatial size of the load, the deformation continues even after the maximum stress point, and this portion of the strain contributes to the permanent deformation. The other metallic material, Stainless Steel A2205, showed a similar behavior, but the strain is much smaller than the curves for the Aluminum. As Aluminum 7075 is softer than Stainless Steel, it undergoes larger strains and deformations compared to the Stainless Steel A2205.

Published in Journal of Materials Science, Vol. 49, Iss. 8, pp. 3034-3051, April 2014
http://link.springer.com/article/10.1007%2Fs10853-013-8002-5

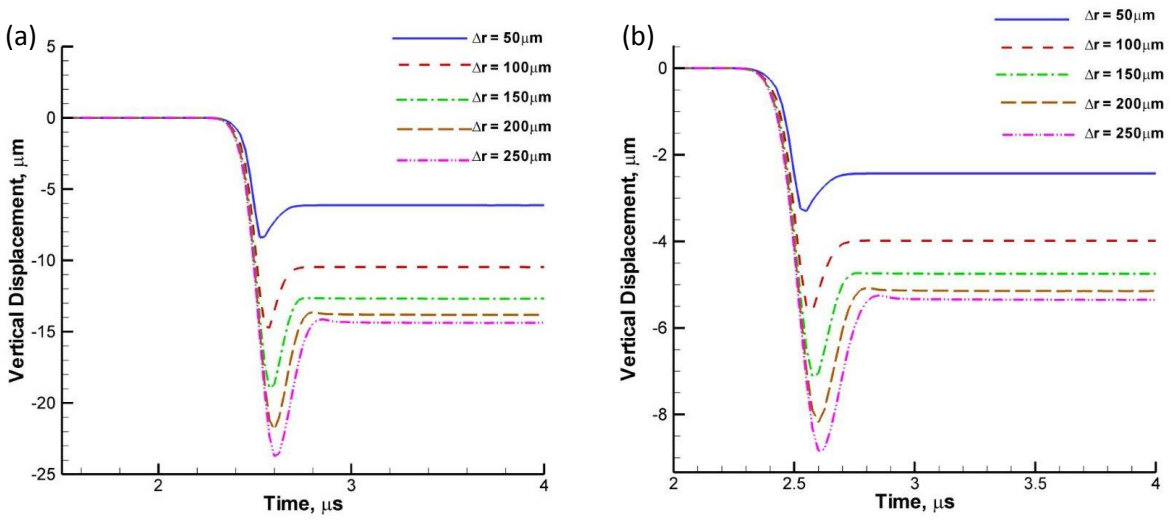

Figure 16. (a) Maximum displacement observed at the center point for Al 7075 and (b) for Stainless Steel A2205, The loading function had the same duration, Δt = 0.1 μs, and same peak pressure P_0 = 2 GPa.

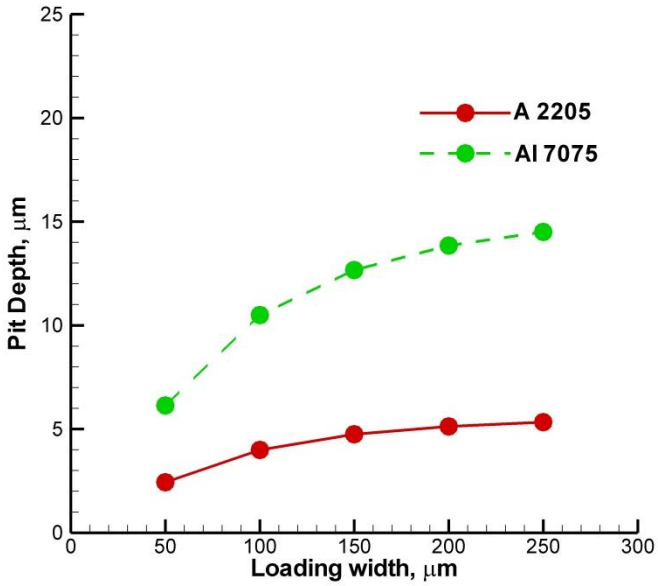

Figure 17. Variation of the pit depth (permanent deformation) with the radial extent of the loading for Aluminum 7075 and Stainless Steel A2205.

Published in Journal of Materials Science, Vol. 49, Iss. 8, pp. 3034-3051, April 2014
http://link.springer.com/article/10.1007%2Fs10853-013-8002-5

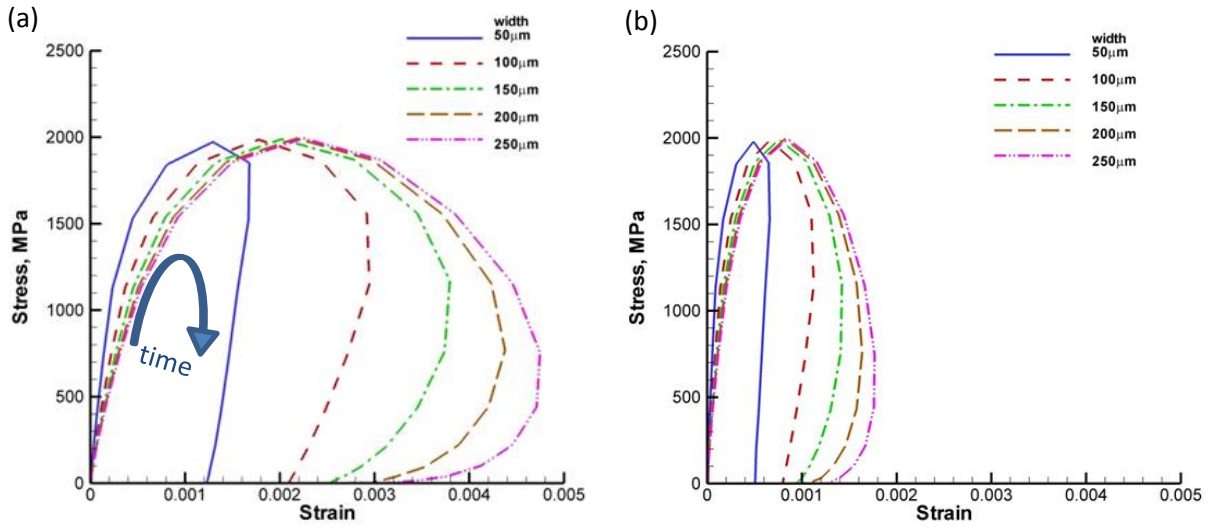

Figure 18. Stress-Strain evolution for a) Aluminum 7075 and b) Stainless Steel A2205 for different loading size. The loading function had the same duration, Δt = 0.1 μs, and same peak pressure P_0 = 2 GPa.

Similar simulations with varying radial extent of the loads were conducted for the compliant materials. The variations of the central point displacement with time for different loading radial extents for Rubber #1 are shown in Figure 19(a). This plot shows that the material surface returns to its original position as the load is removed. As the radial extent of the load increases, the maximum displacement occurs with more delay. The loading part of the displacement followed a common curve regardless of the radial extent, but the unloading started later when the radial extent is increased. Larger size load took more time until the center point returned to the original location. This behavior is shown in the stress-strain space plot in Figure 19 (b). As the radial extent of loading increases, the recovery starts later and later at a larger stain and a smaller stress, and eventually it starts when the stress is very close to zero.

A comparison for all compliant materials for the characteristic loading size of 250 μm is shown in Figure 20. As expected, softer material shows larger strain. Compared to the behaviors of the metals (Figure 18), compliant materials show the beginning of recovery at a very low (near zero) stress level which occurs at the maximum strain. In the case of Polyurea, the start of recovery shows a sharper change compared to the two rubbers we studied. Figure 21 shows the trend of the maximum deformation as the radial extent of the load is varied. As the loading radial extent increased, the maximum vertical displacement increased reaching its maximum as an asymptote. This trend is similar to that observed for the metals earlier (Figure 17).

Published in Journal of Materials Science, Vol. 49, Iss. 8, pp. 3034-3051, April 2014
http://link.springer.com/article/10.1007%2Fs10853-013-8002-5

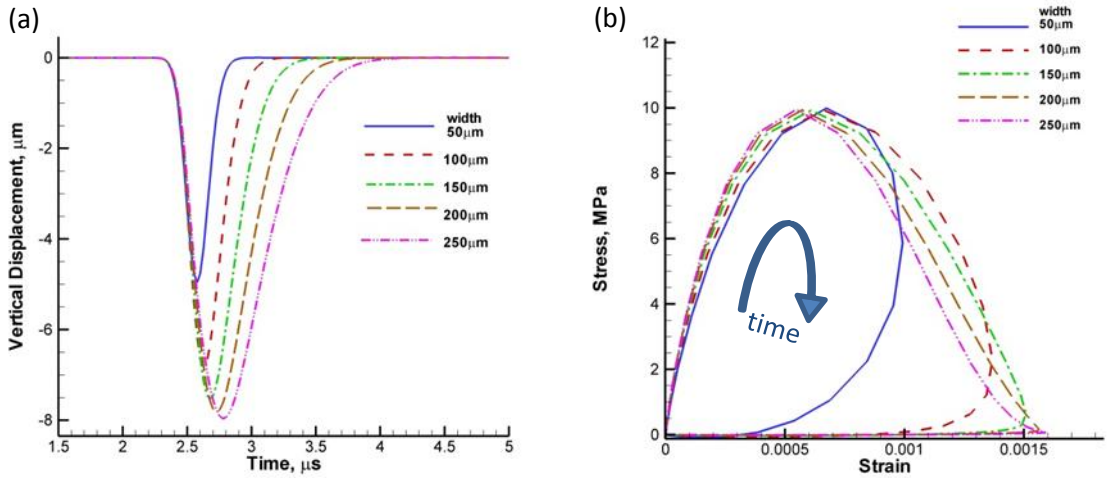

Figure 19. (a) Maximum displacement observed at the center point for Rubber #1, (b) Stress-Strain behavior for Rubber #1 for different loading sizes. The loading function had the same duration, Δt =0.1 μs, and same peak pressure=10 MPa.

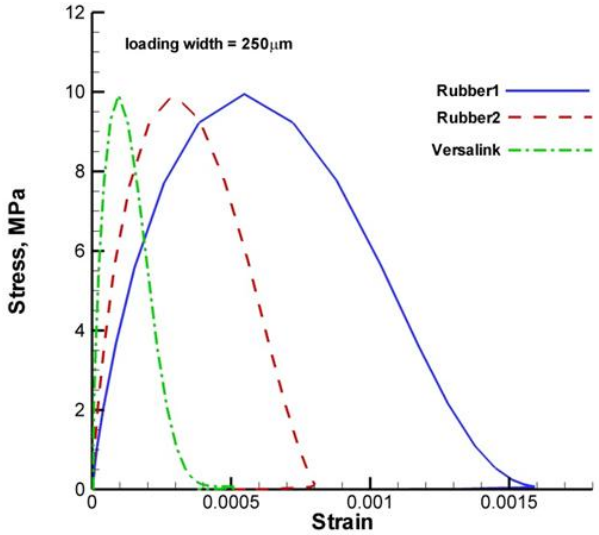

Figure 20. Stress-Strain behavior for the characteristic loading size of 250 μm for all compliant materials. The loading function had the same duration, Δt = 0.1 μs, and same peak pressure of 10 MPa.

Published in Journal of Materials Science, Vol. 49, Iss. 8, pp. 3034-3051, April 2014
http://link.springer.com/article/10.1007%2Fs10853-013-8002-5

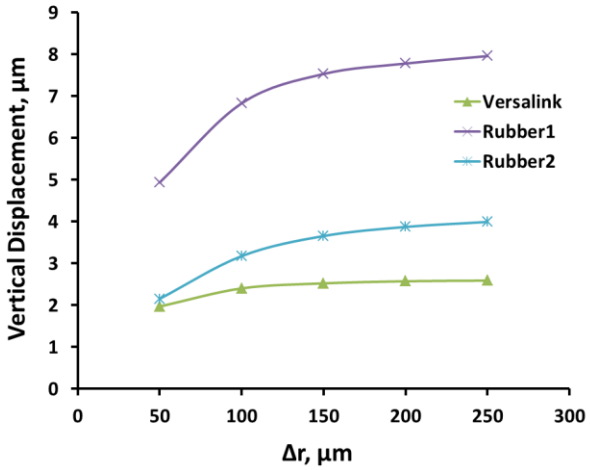

Figure 21. Variation of the maximum vertical displacement of the center point with different radial extent of the applied loads. The loading function had the same duration, Δt = 0.1 µs, and same peak pressure of 10 MPa.

5. Effects of Material Properties on Pitting

Material designers could benefit from understanding how the physical properties of a material such as modulus, yield stress, etc. affect the material response to the cavitation impulsive loads. Identifying the trends and tradeoffs of varying the different material properties would help select materials for better cavitation resistance. In this section a parametric study is presented, which aims at understanding the dependence of pit characteristics on the material properties. An elastic-plastic material model is selected to present simply the trends.

5.1. Stress-Strain Relations in Elastic-Plastic Material Model

For an elastic-plastic model the material parameters of interest are the Young's modulus E, the tangent modulus in the plastic regime E_P, and the yield stress σ_Y. The stress-strain relation, illustrated in Figure 22, can be expressed as follows:

$$\sigma = \begin{cases} E\varepsilon_Y, & \varepsilon \le \varepsilon_Y, \\ E\varepsilon_Y + E_P\left(\varepsilon - \varepsilon_Y\right), & \varepsilon > \varepsilon_Y, \end{cases} \tag{5}$$

where ε_Y is the strain at the yield point, $\sigma_Y = E\varepsilon_Y$.

For a loading, σ_{Load}, which exceeds the yield stress, the permanent strain, ε_∞, remaining after the removal of the load is

$$\varepsilon_\infty = \frac{\sigma_Y}{E} + \frac{\sigma_{Load} - \sigma_Y}{E_P} - \frac{\sigma_{Load}}{E} \tag{6}$$

since unloading occurs along a stress-strain line parallel to the elastic line. The unloading is expressed in the last term of (6) which is the elastic recovery of strain from its maximum.

Published in Journal of Materials Science, Vol. 49, Iss. 8, pp. 3034-3051, April 2014
http://link.springer.com/article/10.1007%2Fs10853-013-8002-5

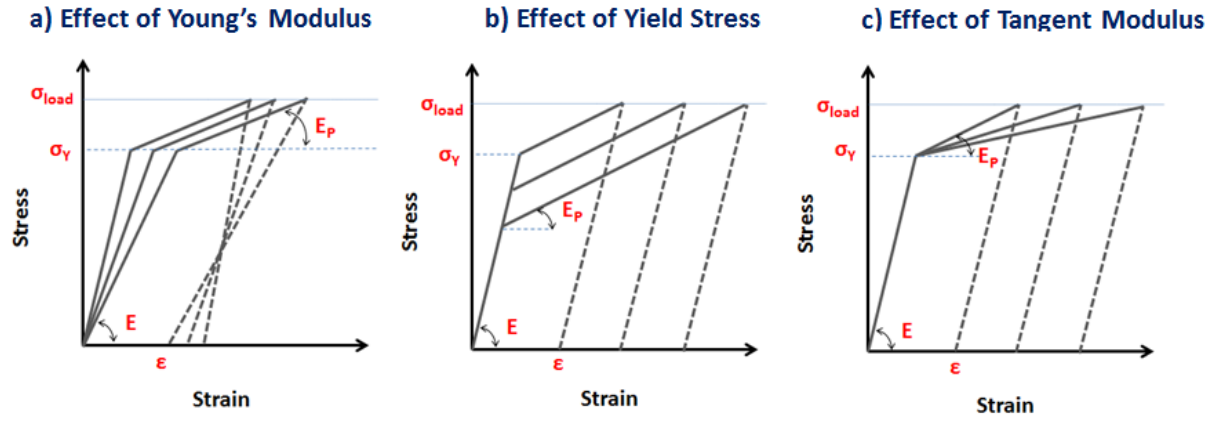

Figure 22. Illustration of the elastic-plastic material behavior and of the three parametric studies changing one parameter at a time: a) varying the Young's modulus, b) varying the yield stress, and c) varying the plastic tangent modulus.

In order to study the effects of the three parameters, E, E_P, and σ_Y, on the generated pitting, a synthetic loading of amplitude 2 GPa, with a duration of 0.25 μs, and a radial extent of 200 μm radius is used, and the above three material parameters were varied. The computational domain and the mesh used are the same as shown earlier in Figure 3. One material parameter is varied at a time while the other two parameters are fixed. The simulation results are described below.

5.1. Sensitivity of the Pit to Young's Modulus

Let us consider for illustration the response of Stainless Steel A2205 (see Table 1) to the above selected impulsive load. The resulting stresses and strains in the material at two instants long after the load was relieved, t = 2.5 μs and t = 10 μs, are shown in Figure 5 and Figure 6 respectively. Both figures illustrate that in practice the load affects only a limited finite volume of the material below the area of application of the load. This is illustrated further in the following quantitative plots.

Figure 23a shows the variation with the depth of the effective stress at the axis of symmetry directly beneath the loading area. Two times are selected to show the depth function; the first is at the time when the stresses in the material reach a maximum, and the second at a much later time, where only residual effects can be seen. The effective stress at t = 2.5 μs shows interestingly that the material experiences an almost constant stress slightly above the yield stress of the material (515 MPa) between depths of 40 μm to 400 μm. This whole region (see Figure 5 for the distribution of the stress in space) inside the material experiences plastic deformation. The residual stress (or the effective stress) at the later observation time, t = 10 μs, still shows a stress plateau but of a smaller physical extent and with a stress level below the yield stress.

Figure 23b shows, for comparison, the effective stress distribution for a material which has a 50 GPa Young's modulus. With this lower value of the Young's modulus than for the

Published in Journal of Materials Science, Vol. 49, Iss. 8, pp. 3034-3051, April 2014
http://link.springer.com/article/10.1007%2Fs10853-013-8002-5

Stainless Steel A2205 (E=190GPa), the equivalent strain at the maximum load (t = 2.5 μs) exceeds further the yield stress but still within the same 40 μm to 400 μm depth region. However, the stress level at the final time recovers to a much lower value than the A2205, 300 MPa versus500 MPa. This behavior can be explained intuitively through the sketch in Figure 22a, where one can see that, for fixed E_p, and σ_Y, the value of the permanent strain is seen to decrease as the slope E decreases. The lower Young's modulus material recovers more from the maximum stress level the material has experienced because it has larger recoverable strain energy under the elastic regime for the same given yield stress. It is important to note that for both values of E, the maximal stresses felt by the material (in the depth region 40-400 μm) are significantly lower than the applied load: 550 MPa and 560 MPa versus 2GPa. This is very important to remember for studies of cavitation pitting [38]. Also for both Young's moduli, it can be observed that most of the plastic strain occurs within the upper half (depth less than 250 μm) of the total hardened thickness. This observation will be used later to estimate the pit depth.

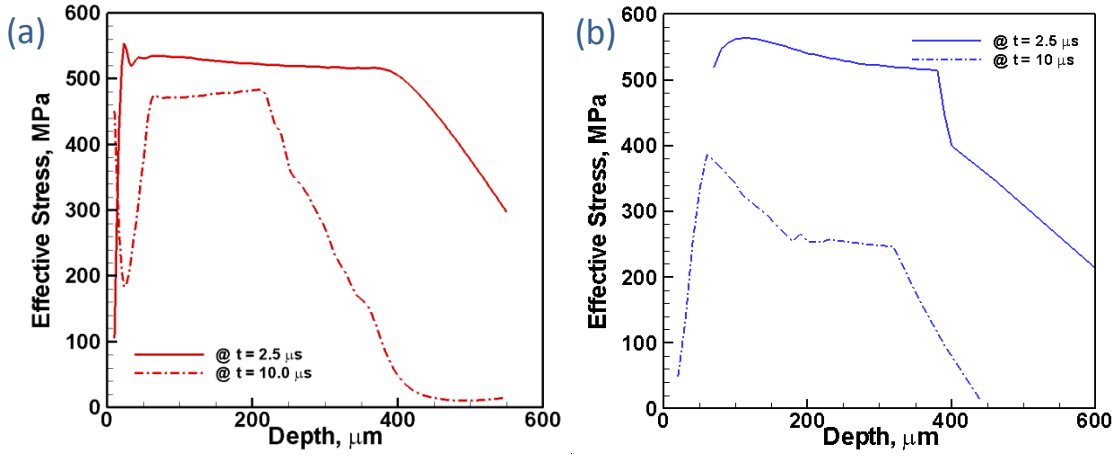

Figure 23. Distribution of the effective stress along the axis of symmetry of the applied load at two instants (at maximum load t=2.5 μs, and at t=10 μs) for: a) Stainless Steel A2205 with E = 190 GPa and b) a material with same σ_Y and E_P and E = 50 GPa. σ_Y = 515 MPa, E_P = 705 MPa. Applied load: P_0 = 2 GPa, Δt = 0.25 μs, Δr = 200 μm.

Figure 24 shows, for the same two materials as in Figure 23, the equivalent plastic strain remaining in the material as permanent deformation at t = 10 μs. Both residual plastic strain curves peak at a depth of 100 μm. The material with a lower Young's modulus results in a larger residual plastic strain, which is a result of a larger overall deformation during the loading event. These curves show that the selected loading affected the material down to about a depth of 400 μm, which is the thickness of the hardened layer of the material after the cavitation loading. Note that this depth is affected only slightly by the Young's modulus.

Published in Journal of Materials Science, Vol. 49, Iss. 8, pp. 3034-3051, April 2014
http://link.springer.com/article/10.1007%2Fs10853-013-8002-5

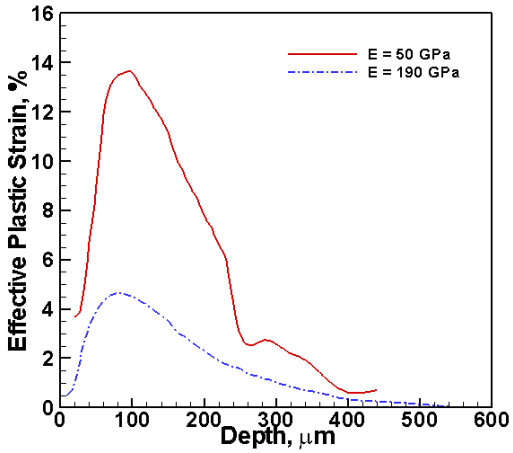

Figure 24. Distribution of the equivalent plastic strains at the final stage (t = 10 μs) for the two materials with Young's moduli, E = 190 GPa and E = 50 GPa. σ_Y = 515 MPa, E_P = 705 MPa. Applied load: P_0 = 2 GPa, Δt = 0.25 μs, Δr = 200 μm.

To study more systematically the effects of the Young's modulus, we consider the same load and a set of *E* values between 50 GPa and 190 GPa. The other two material parameters are kept fixed: σ_Y = 515 MPa and E_P = 705 MPa (the values for the Stainless Steel A2205). The pit depth, maximum effective stress, and the hardened depth are extracted from the simulations and shown in Figure 25.

Figure 25a shows that as the Young's modulus increases, the hardened depth increases and the maximum effective stress decreases. However, these changes are very moderate; less than 10% for an almost fourfold modulus increase. These trends can be explained as follows. As the Young's modulus increases, the strain energy per unit volume of material contained under the stress-strain curve becomes smaller for the same maximum load level. As a result, the energy from the same loading needs a larger material volume to be absorbed. Thus, the affected hardened layer thickness becomes a little larger.

The observed trend can be recovered analytically by considering the relationships presented in Figure 22a as follows. When the yield stress, the tangent modulus, and the load are kept the same, and only the Young's modulus is varied, the relationship between the resulting permanent strain, ε_∞, and the Young's modulus is of the type $\varepsilon_\infty \approx E^{-1}$ and can be expressed as:

$$\varepsilon_\infty(E) = \alpha_1 - \frac{\alpha_2}{E}, \quad \text{with} \quad \alpha_1 = (\sigma_{Load} - \sigma_Y)\frac{1}{E_P}, \qquad \alpha_2 = \sigma_{Load} - \sigma_Y . \tag{7}$$

Note that all stress-strain recovery lines (dashed lines in Figure 22a) cross at a single point $(\varepsilon_\times, \sigma_\times)$ described by the following expression:

$$\varepsilon_\times = \frac{1}{E_P}(\sigma_{Load} - \sigma_Y), \qquad \sigma_\times = \sigma_{Load} - \sigma_Y . \tag{8}$$

Published in Journal of Materials Science, Vol. 49, Iss. 8, pp. 3034-3051, April 2014
http://link.springer.com/article/10.1007%2Fs10853-013-8002-5

Expression (7) matches the experimental results when the maximum stress σ_{Load}, to be used in the expressions of α_1 and α_2, is properly selected. As noted earlier, σ_{Load} is much smaller than the imposed synthetic load. Here we will use the values from the maximum effective stress shown in Figure 25a. The corresponding value of the strain is then calculated simply by:

$$\varepsilon_\infty = \left(\frac{1}{E_P} - \frac{1}{E}\right)\left(\sigma_{\max} - \sigma_Y\right), \tag{9}$$

and this strain can be converted to the pit depth, d_{pit}, noting, from observation of the solution results, that the deformation occurred mostly in the upper 50% of the total hardened thickness, T_{hard}:

$$d_{pit} = \varepsilon_\infty \cdot 0.5\, T_{hard}\,. \tag{10}$$

The pit depth calculated by (10) is compared with the direct value from the simulation on the right plot of Figure 25b. The agreement is quite good, and the same procedure could be used to estimate simply the pit depth from the material property.

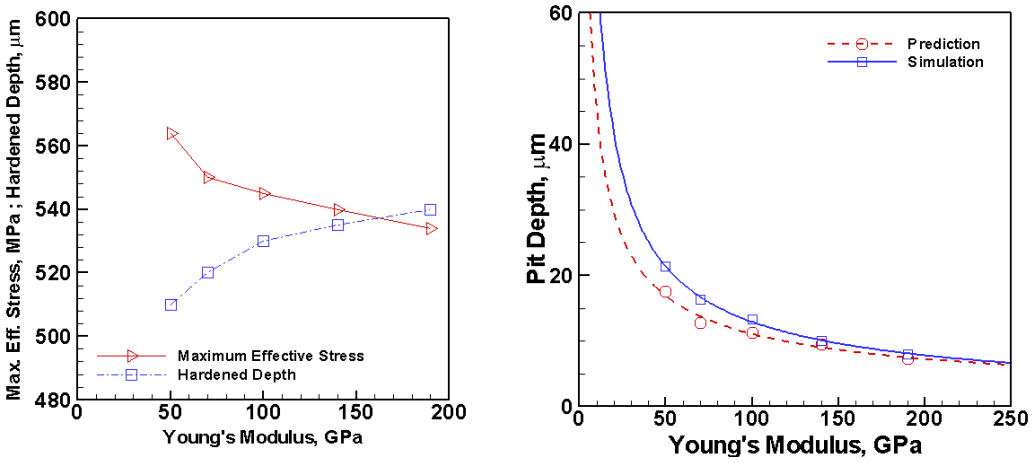

Figure 25. Effect of the material Young's modulus on: a) the maximum effective stress experienced by the material and b) the pit depth. σ_Y = 515 MPa, E_P = 705 MPa, P_0 = 2 GPa, Δt = 0.25 μs, Δr = 200 μm.

5.2. Sensitivity of the Pit to the Yield Stress

To study the sensitivity to the yield stress, the Young's and tangent moduli are fixed and the yield stress of the material is varied (See Figure 22b). In this case, the permanent strain in (6) can be rewritten as a function of yield stress as follows:

$$\varepsilon_\infty\left(\sigma_Y\right) = \alpha_3 - \alpha_4\sigma_Y, \quad \text{with} \quad \alpha_4 = \left(\frac{1}{E_P} - \frac{1}{E}\right), \qquad \alpha_3 = \alpha_4\sigma_{Load}, \tag{11}$$

illustrating that the permanent strain behaves as a linear function of the yield stress.

Published in Journal of Materials Science, Vol. 49, Iss. 8, pp. 3034-3051, April 2014
http://link.springer.com/article/10.1007%2Fs10853-013-8002-5

In order to observe the effects of the yield stress, the two moduli are selected as E = 190 GPa and E_p = 705 MPa (the values for Stainless Steel A2205), and the yield stress is varied from 250 MPa to 750 MPa. From curves like those in Figure 23 for each yield stress, the pit depth (i.e. permanent displacement of the surface center point), the maximum effective stress, and the hardened depth (i.e. the deepest depth where measurable plastic strain occurred) are measured. These are summarized in Figure 26a. As expected, the pit depth and the hardened layer thickness decrease when the yield stress increases. The maximum effective stress in the material, on the other hand, increases as the yield stress increases. This reflects again the earlier observation that the maximum stress felt by the material is very close to the yield stress of the material. Any excess stress from the loading would be therefore relieved through straining of the volume around the impact zone.

The predicted depth by (11) is compared with the computed depth from the simulation on the right plot of Figure 26. The agreement is again very good, and it can be concluded that the pit depth decreases as the yield stress increases as a result of the two competing effects of increasing effective stress and decreasing hardened depth.

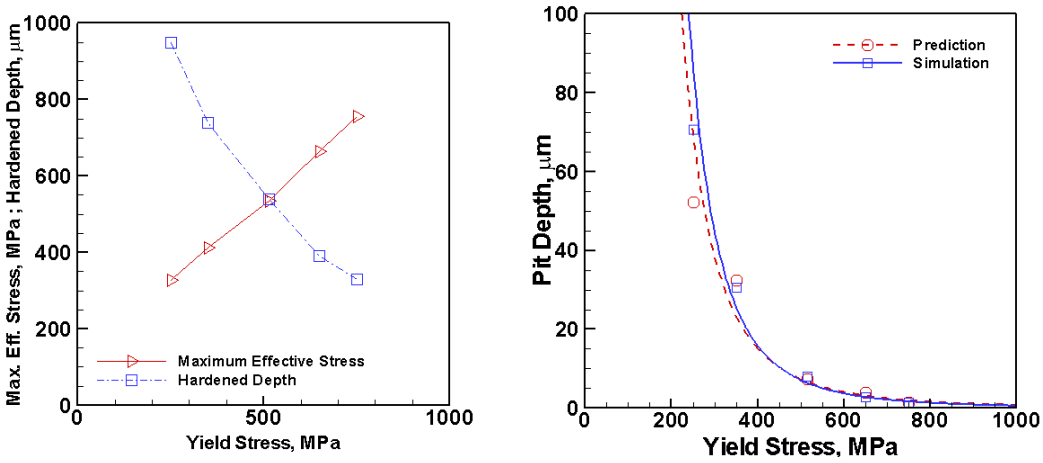

Figure 26. Effect of the material Young's modulus on: a) the maximum effective stress experienced by the material and b) the pit depth. E = 190 GPa, E_P = 705 MPa, P_0 = 2 GPa, Δt = 0.25 μs, Δr = 200 μm.

5.3. Sensitivity of the Pit to the Plastic Modulus

If the yield stress and the Young's modulus are assumed the same, and only the tangent modulus is varied, the resulting permanent strain can be expressed as

$$\varepsilon_\infty\left(E_p\right)=\frac{\alpha_1}{E_p}-\alpha_5, \quad \text{with} \quad \alpha_5=\left(\sigma_{Load}-\sigma_Y\right)\frac{1}{E}. \tag{12}$$

In order to observe the effects of the plastic tangent modulus, the other two parameters were fixed at σ_Y = 515 MPa and E = 190 GPa (the values for Stainless Steel A2205) and the plastic tangent modulus was varied from 200 MPa to 1,500 MPa. The resulting pit depth, maximum effective stress, and thickness of the hardened layer are summarized in Figure 27. We

can see that the hardened depth is little affected by the plastic tangent modulus. On the other hand, as the plastic modulus increases the pit depth decreases, which is expected as the plastic deformation is inversely proportional to the plastic modulus, and the maximum effective stress increases. This can be explained by the fact that the maximum stress in the material is higher as the material becomes stiffer.

The pit depth calculated by (12) for this set of simulations again compares well with the direct values from the simulations as seen in Figure 27b.

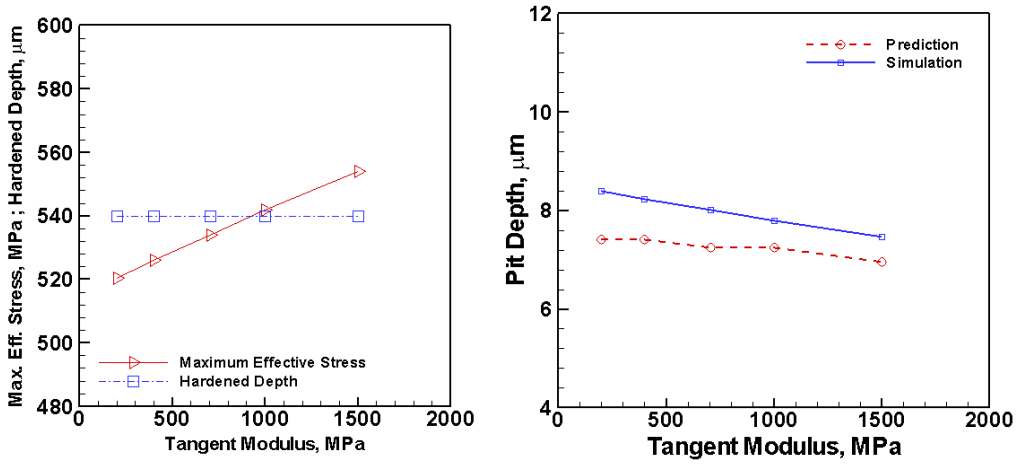

Figure 27. Effect of the material plastic tangent modulus on: a) the maximum effective stress experienced by the material and b) the pit depth. σ_Y = 515 MPa, E = 190 GPa, E_P = 705 MPa, P_0 = 2 GPa, Δt = 0.25 μs, Δr = 200 μm.

6. Conclusions

Using synthetic pressure loads corresponding to typical impulsive pressure loads in a cavitation field, we studied the response of various metallic and compliant materials. For the selected loads and materials properties (i.e. elastic plastic for metals) pitting (i.e. permanent plastic deformation) could be computed in the metals when the effective stresses exceed the material's yield stress. Pitting was also shown to depend on the loading rate and on the loading lateral extent.

The material response followed the timing of the pressure loading during the loading part of the curve. However, the unloading part showed major differences among the materials. For metals, the final permanent depth was independent of the duration of the loading when the loading was applied slower than a certain time scale. However, if the loading was faster than this time scale, the permanent depth became deeper up to a certain time scale as the loading was applied faster. When the duration of the applied load was too short, the pit depth reduced. Compliant materials, however, showed increased maximum deformation with the loading duration. The trend was nonlinear, and the maximum deformation saturated as the loading time became longer. Polyurea, a viscoelastic material, required much longer time for full recovery than the hyper-elastic rubbers and deformed more as the loading duration increased.

The radial extent of the load also affected the pit depth. There was an increase in the maximum deformation with the increase of the loading radial extent. Permanent deformation for metals increased with the increase of the radial extent. As the loading area increased the stress recovery for compliant materials was delayed until the strain was at its maximum and the stress was very close to zero. In the case of Polyurea, the start of recovery was quite extreme showing a very sharp change in the stress-strain space compared to the two rubbers studied.

For a given cavitation impulsive load, the effect of the material parameters of an elastic-plastic material was also studied numerically to evaluate pit size and thus cavitation erosion resistance. The cases studied showed that the plastic modulus has the least influence on the pit depth when compared to the effect of the Young's modulus and the yield stress. Pit depths are substantially affected by and inversely proportional to both the yield stress and the Young's modulus. In terms of the thickness of the hardened layer, a higher yield stress will decrease the hardened thickness, while a higher Young's modulus will increase the hardened thickness. The plastic modulus was found to not affect the hardened thickness.

Use of synthetic loading in this study enabled a relatively simple evaluation of the response of different materials for different load characteristics and provided us a better understanding of the pit characteristics relative to the pressure loading magnitude, duration, and radial extent. This study revealed that the depth of the pit is a result of not only the magnitude of the loads but also of a combination of the loading duration and spatial size. In order to build a correlation between the pitting test results and the cavitation fields in our future studies, we need a further knowledge regarding the loads generated by the cavitation bubble collapses.

7. Acknowledgement

This work was supported by DYNAFLOW and by the Office of Naval Research under Contract N00014-11-C-0378, monitored by Dr. Ki-Han Kim. We gratefully acknowledge this support.

8. References

1. Chahine GL, Franc JP, Karimi A (2014) Ch. 1 Cavitation and cavitation erosion In: Advanced experimental and numerical techniques for cavitation erosion prediction. ed. Kim KH, Chahine GL, Franc JP, Karimi A. Springer. (book in press)
2. Pereira F, Avellan F, Dupont Ph (1998) Prediction of cavitation erosion: an energy approach. Journal of Fluids Engineering **120:**719-727.
3. March PA (1987) Evaluating the relative resistance of materials to cavitation erosion: a comparison of cavitating jet results and vibratory results. Proc. Cavitation and Multiphase Flow Forum, ASME Cincinnati.
4. Soyama H, Lichtarowicz A, Momma T, Williams EJ (1998) A new calibration method for dynamically loaded transducers and its application to cavitation impact measurement. J. Fluids Eng. **120**:712-718.
5. Hattori S, Takinami M, Tomoaki O (2009) Comparison of cavitation erosion rate with liquid impingement erosion rate. 7th Int. Symposium on Cavitation, CAV2009 Ann Arbor, Michigan.

6. Ahmed SM, Hokkirigawa K, Ito Y, Oba R (1991) Scanning electron microscopy observation on the incubation period of vibratory cavitation erosion. Wear **142**:303-314.
7. Bregliozzi G, Di Schino A, Ahmed SI-U, Kenny JM, Haefke H (2005) Cavitation wear behavior of austenitic stainless steels with different grain sizes, Wear **258**:503-510.
8. Dular M, Coutier-Delgosha O (2009) Numerical modeling of cavitation erosion. Int. J. Numer. Meth. Fluids **61**:1388–1410.
9. Blake JR, Taib BB, Doherty G (1986) Transient cavities near boundaries. Part I. rigid boundary. Journal of Fluid Mechanics **170**:479-497.
10. Zhang H, Duncan J, Chahine GL (1993) The final stage of the collapse of a cavitation bubble near a rigid wall, Journal of Fluid Mechanics **257**:147-181.
11. Chahine GL, Perdue TO (1988) Simulation of the three-dimensional behavior of an unsteady large bubble near a structure, Drops and Bubbles, Third International Colloquium, Monterey, CA, ed. Taylor G. Wang. American Institute of Physics. 188-199.
12. Lush PA (1983) Impact of a liquid mass on a perfectly plastic solid. J. Fluid Mech. **135**:373–387.
13. Thiruvengadam A (1974) Handbook of cavitation erosion. Hydronautics Technical Report 7301-1.
14. Eisenberg P, Preiser HS, Thiruvengadam A (1965) On the mechanisms of cavitation damage and methods of protection. Trans. Soc. Naval Architects Marine Eng. **73**:241–286.
15. Dominguez Cortazar MA, Cavermod L (1992) Modèle Physique de l'érosion de cavitation: qualification expérimentale et numérique, Thèse Université Joseph Fourier Grenoble I.
16. Reboud JL (1987) Réponse Impulsionnelle d'un milieu elastoplastique: application a l'étude de l'érosion de cavitation, Thèse, Institut National Polytechnique de Grenoble.
17. Parsons CA, Cook SS (1919) Investigation into causes of corrosion or erosion of propellers. J. Am. Soc. Naval Eng., **31**:536-541.
18. Plesset MS, Ellis AT (1955) On the mechanism of cavitation damage. Trans. ASME, **77**:1055-1064.
19. Knapp RT (1955) Recent investigations of the mechanics of cavitation and cavitation damage. Trans. ASME, **77**:1045-1054.
20. Knapp RT (1958) Accelerated field tests of cavitation intensity. Trans. ASME, **80**:91-102.
21. Knapp RT, Daily JW, Hammitt FG (1970) Cavitation. McGraw-Hill, London.
22. Dorey JM, Laperrousaz E, Avellan P, Dupont P, Simoneau R, Bourdon P (1996) Cavitation erosion prediction on Francis turbines – Part 3 methodologies of prediction. Hydraulic machinery and cavitation: proc. the XVIII IAHR Symposium. ed. Cabrera, E., Espert, V. Martinez, F. Vol. I, Kluwer Academic Publishers.
23. Dular M, Stoffel B, Sirok B (2006) Development of a cavitation erosion model. Wear **261**:642-655.
24. Berchiche N, Franc J-P, Michel JM (2001) A cavitation erosion model for ductile materials. Proc. 4th International Symposium on Cavitation, CAV2001. Pasadena, CA.
25. Farhat M, Bourdon P, Lavigne P, Simoneau R (1997) The Hydrodynamic aggressiveness of cavitating flows in hydro turbines. ASME Fluids Engineering Division Summer Meeting, FEDSM'97.
26. Billet ML (2005) The specialist committee on cavitation erosion on propellers and appendages on high powered/high speed ships. Final report and recommendations to the 24th ITTC. Proc. 24th Int. Towing Tank Conference. Vol. II.

27. Stinebring DR, Holl JW, Arndt REA (1980) Two aspects of cavitation damage in the incubation zone: Scaling by energy considerations and leading edge damage. J. Fluid Engineering **102**:481-485.
28. Lee MK, Hong SM, Kim GH, Kim KH, Rhee CK, Kim WW (2006) Numerical correlation of the cavitation bubble collapse load and frequency with the pitting damage of flame quenched Cu-9Al-4.5Ni-4.5Fe alloy. Materials Science & Engineering A (Structural Materials: Properties, Microstructure and Processing) **425**(1-2):15-21. doi:10.1016/j.msea.2006.03.039
29. Hattori S, Takinami M, Otani T (2009) Comparison of cavitation erosion rate with liquid impingement erosion rate. Proc. 7th Int. Symposium on Cavitation. Ann Arbor, Michigan, USA.
30. Whirley RG, Engelmann BE (1993) DYNA3D: A nonlinear, explicit, three dimensional finite element code for solid and structural mechanics - user manual. Lawrence Livermore National Laboratory. UCRL-MA-107254, Rev. 1.
31. Lin JI (2005) DYNA3D: A nonlinear, explicit, three-dimensional finite element code for solid and structural mechanics. User manual. Laurence Livermore National Laboratory. UCRL-MA-107254.
32. Amirkhizi AV, Isaacs J, McGee J, Nemat-Nasser S (2006) An experimentally-based viscoelastic constitutive model for polyurea, including pressure and temperature effects. Philosophical Magazine **86**(36):5847-5866.
33. (2010) Polyurethane Properties. American Urethane, Inc. http://americanurethane.com/polyurethane-properties.html.
34. (2013) Neoprene Technical Data Sheets. MatWeb.com. http://www.matweb.com/search/GetMatlsByTradename.aspx?navletter=N&tn=Neoprene.
35. Jayaprakash A, Hsiao C-T, Chahine GL (2012) Numerical and experimental study of the interaction of a spark-generated bubble and a vertical wall. Trans. ASME, J. Fluid Engineering **134**:031301.
36. Singh S, Choi J-K, Chahine GL (2013) Characterization of cavitation fields from measured pressure signals of cavitating jets and ultrasonic horns. J. Fluid Engineering **135**:9. doi: 10.1115/1.4024263
37. Jayaprakash A, Choi J-K, Chahine GL, Martin F, Donnelly M, Franc J-P, Karimi A (2012) Scaling study of cavitation pitting from cavitating jets and ultrasonic horns. Wear **296**:619-629.
38. Chahine GL (2014) Ch. 6 Modeling of cavitation dynamics and interaction with material In: Advanced experimental and numerical techniques for cavitation erosion prediction. ed. Kim KH, Chahine GL, Franc JP, Karimi A. Springer. (book in press)